RSC Advances

PAPER

View Article Online
View Journal | View Issue

Open Access Article. Published on 12 Mac 2019. Downloaded on 3/09/2025 6:27:22 PTG.
This article is licensed under a Creative Commons Attribution-NonCommercial 3.0 Unported Licence.

Check for updates

Cite this: *RSC Adv.*, 2019, **9**, 8280

Nanocomposite functionalized membranes based on silica nanoparticles cross-linked to electrospun nanofibrous support for arsenic(v) adsorption from contaminated underground water†

L. Yohai,*[a] H. Giraldo Mejía,[a] R. Procaccini,[a] S. Pellice,[a] K. Laxman Kunjali,[b] J. Dutta[b] and A. Uheida*[b]

Nanocomposite functionalized membranes were synthesized using surface functionalized mesoporous silica nanoparticles (MCM-NH_2 or MCM-PEI) cross-linked to a modified polyacrylonitrile (mPAN) nanofibrous substrate for the removal of 1 mg L^{-1} of As(v); a concentration much higher than what has been reported for underground water in Argentina. Adsorption studies were carried out in batch mode at pH 8 with nanoparticles in colloidal form, as well as the nanoparticles supported on the modified PAN membranes (mPAN/MCM-NH_2 and mPAN/MCM-PEI). Results indicate a twenty-fold improvement in As(v) adsorption with supported nanoparticles (nanocomposite membranes) as opposed to their colloidal form. The adsorption efficiency could be further enhanced by modifying the nanocomposite membrane surface with Fe^{3+} (mPAN/MCM-NH_2-Fe^{3+} and mPAN/MCM-PEI-Fe^{3+}) which resulted in more than 95% arsenic being removed within the first 15 minutes and a specific arsenic adsorption capacity of 4.61 mg g^{-1} and 5.89 mg g^{-1} for mPAN/MCM-NH_2-Fe^{3+} and mPAN/MCM-PEI-Fe^{3+} nanocomposite membranes, respectively. The adsorption characteristics were observed to follow a pseudo-first order behavior. The results suggest that the synthesized materials are excellent for quick and efficient reduction of As(v) concentrations below the WHO guidelines and show promise for future applications.

Received 30th November 2018
Accepted 25th February 2019

DOI: 10.1039/c8ra09866b

rsc.li/rsc-advances

1. Introduction

Arsenic (As) is an abundant element on earth, widely distributed in water, air, rocks and soil. The presence of arsenic in the environment occurs because of both natural and anthropogenic activities.[1] Arsenic exists in its inorganic and organic forms, however, dissolved species of As in water are mainly inorganic, arsenite being the dominant form under reducing conditions and arsenate the most stable species in oxygenated environments.[2] Organic forms of arsenic, mostly found in fishes and crustaceans, are believed to be non-toxic. Exposure of the general population to As primarily occurs through groundwater consumption and, in addition, there is a risk of exposure in human health due to the introduction of arsenic into the food chain through crops, rice, milk, meat and others.[3,4] The most affected countries are India, Bangladesh, China, Japan, Taiwan, Canada, USA, Mexico, Chile and Argentina. Inorganic arsenic is classified as a carcinogenic and neurotoxic contaminant. Long-term arsenic exposures can cause skin, kidney, liver and bladder cancers. Arsenic exposure can also manifest in other outcomes such as hypertension, diabetes and heart diseases.[3] In 2011, the World Health Organization (WHO) and the United States Environmental Protection Agency (US EPA) recommended a maximum tolerable limit of 0.01 mg L^{-1} of As in drinking water.[2,5,6] In Argentina, it is common to find many citizens affected by chronic endemic regional hydroarsenism (H.A.C.R.E., letters due to words in Spanish) characterized by dermal lesions on palms and feet.[7] This kind of disease is related to the consumption of water contaminated with an As concentration exceeding WHO's recommended limit. More than 4 million Argentinian citizens are exposed to water and groundwater contaminated with As. The most affected regions in Argentina are the provinces of La Pampa, Tucumán, Córdoba, Santa Fe, Chaco, Santiago del Estero and Salta.[8–11] In Buenos Aires province, 87% of water and groundwater analysis have shown arsenic concentrations far beyond the concentrations recommended for drinking water.[12] In the rural areas, for example the city of Rafaela, which is the main milk producing region of Santa Fe, arsenic concentrations in water between 0.18 and 0.32 mg L^{-1} have been found.[13]

Several technologies are used to reduce arsenic concentrations to safe limits, such as co-precipitation, oxidation/

[a]División Cerámicos, INTEMA, CONICET, UNMdP, B7608FDQ Mar del Plata, Argentina. E-mail: yohai@fi.mdp.edu.ar

[b]Functional Materials Group, Department of Applied Physics, KTH Royal Institute of Technology, 16440 Kista, Stockholm, Sweden. E-mail: salam@kth.se

† Electronic supplementary information (ESI) available. See DOI: 10.1039/c8ra09866b

 This journal is © The Royal Society of Chemistry 2019

Open Access Article. Published on 12 Mac 2019. Downloaded on 3/09/2025 6:27:22 PTG.
This article is licensed under a Creative Commons Attribution-NonCommercial 3.0 Unported Licence.

filtration, selective adsorption, reverse osmosis, ion exchange, activated alumina, coagulation/filtration, photocatalysis and nanofiltration.[6] Adsorption has been widely used being simple, inexpensive and efficient technology for treatment of ground and wastewater, air emissions or for removing a series of toxic chemicals and heavy metals.[14] Adsorbents such as carbon nanospheres,[15] metal oxide nanoparticles,[16–19] carbon nanotubes (CNTs),[20–22] Fe species such as Fe, Fe_2O_3, Fe_3O_4 (ref. 23–26) and mesoporous silica nanoparticles[23,27–29] have been employed to remove arsenic from contaminated water.

Mesoporous silica nanoparticles have caught attention due to its unique properties like large surface area, high pore volume, ordered structure, chemical versatility and good mechanical and thermal stability. In addition, it is possible to functionalize silanol groups present in the structure with amine groups.[24] In particular, MCM-41 is an ordered mesoporous silica characterized by a two dimensional hexagonal array of cylindrical pores.[28,30] MCM-41, with high density of amino groups and well-defined mesochannels, can enhance the accessibility of molecules capable of adsorb cations, such as cobalt, copper, zinc and arsenic. The adsorbents, however, tend to aggregate into larger particles, leading to lower adsorption capacity due to reduction of surface area. The use of supporting materials, such as nanofibers and carbon nanotubes, can improve the adsorptive performance of nanoparticles due to the distribution of these particles on its surfaces.[31] Nanofibrous membranes have small fiber diameters that lead to large specific surface area and high flexibility for chemical/physical surface functionalization.[32] The use of nanofibrous membranes is favored over other technologies for water treatment due to lower energy consumption, high selectivity and continuous mode operation possibilities.[33] Polyacrylonitrile (PAN) nanofibers are popular due to its excellent mechanical properties, commercial availability, environmental stability and chemical versatility. Nitrile groups on PAN surface can be modified through simple chemical reactions to be easily cross-linked with polyamines.[5] Recently, the use of nanocomposite materials has become a novel and promising technology for water remediation. Particularly, one successful technique is to add nanoparticles to polymeric or ceramic membranes during membrane synthesis.[34]

In this study, we developed nanocomposite membranes for efficient removal of As(v). For this purpose, As(v) adsorption studies were carried out with amino functionalized nanoparticles (NPs) cross-linked to a support of modified polyacrylonitrile nanofibers (mPAN). The attachment of Fe^{3+} to the nanocomposite nanofibers membranes was also evaluated for arsenic removal efficiency. Experiments were performed in the batch mode at pH 8 with constant initial arsenic concentration, 1 mg L^{-1}, higher concentration than what is found in contaminated Argentinian groundwater. Kinetic behavior was studied to evaluate the adsorption process. Techniques such as High Resolution Transmission Electron Spectroscopy (HR-TEM), Scanning Electron Microscopy (SEM), Fourier Transform Infrared Spectroscopy (FTIR) and Zeta Potential (ZP) were used for characterization. Inductively coupled plasma-atomic emission spectroscopy (ICP-OES) was used to quantify As(v) concentration.

2. Materials and methods

2.1. Chemical and materials

Polyacrylonitrile powder (PAN, MW = 150 000 g mol^{-1}), *N*,*N*-dimethylformamide (DMF), tetraethylorthosilicate (TEOS), aminopropyltriethoxysilane (APTES), HCl 37% wt, cetyltrimethylammonium bromide (CTAB), hydroxylamine hydrochloride ($NH_2OH \cdot HCl$), NH_4OH 25% wt, $Fe(NO_3)_3 \cdot 9H_2O$, $Na_2HAsO_4 \cdot 7H_2O$, Na_2CO_3, absolute ethanol, toluene and glutaraldehyde (GA) 50%, were purchased from Sigma-Aldrich. Branched polyethylenimine (PEI, MW = 10 000 g mol^{-1}) was purchased from Alfa-Aesar. All chemicals were analytical grade and were directly used without further purification. High purity water with a resistivity of 15 MΩ cm^{-1} was used in all the experiments.

2.2. Synthesis of the adsorbents

MCM-41 synthesis. Mesoporous silica, MCM-41 type, was obtained by hydrolytic condensation in basic media. 3.09 g of CTAB was mixed with 123 mL of deionized (DI) water, 51.6 g of absolute ethanol and 18.2 mL of NH_4OH 25%. The mixture was stirred for 30 min at room temperature followed by the addition of 4.08 mL of TEOS dropwise and stirred again for 35 s. 576 mL of DI water was then added to dilute and stirred for 3 more min. TEOS condensation was stopped by changing the pH to 9 with 30 mL of HCl/H_2O (1 : 3) solution. Particles were recovered by centrifugation, washed several times with DI water and dried at 80 °C overnight. Mesoporous silica nanoparticles were then calcined at 550 °C for 5 h to remove the surfactant with a ramp of 5 °C min^{-1} during heating or cooling.

MCM-41 surface functionalization. Before functionalization, synthesized MCM-41 nanoparticles were activated in order to enhance free Si–OH groups for the crosslinking step. 0.5 g of calcined MCM-41 were immersed in 20 mL of a 0.7 mol L^{-1} HCl solution overnight and then washed with DI water until pH 7.

Two types of amino precursors were used for surface functionalization: APTES and branched PEI.

APTES functionalization. Activated NPs were refluxed in 100 mL of dry toluene containing 0.85 mL of APTES during 4 h at 100 °C. These nanoparticles were labeled as MCM-NH_2.

PEI functionalization. Activated NPs were functionalized with PEI to enhance amino groups in the adsorbent. Two steps were followed. First, 0.1 g of MCM-NH_2 nanoparticles were mixed with 0.32 g of GA solution. DI water was added to reach 10 g of total solution. After mixing overnight at room temperature, NPs were centrifuged and washed several times with DI water to remove any excess of unreacted GA. After air-drying, 0.075 g of these NPs were mixed with 6.5 g of branched PEI and 20 mL of DI water and stirred overnight at 50 °C. After washing several times with DI water, NPs were vacuum-dried at 60 °C. These NPs were labeled as MCM-PEI.

Electrospinning of PAN and its surface functionalization. A 10% wt solution of PAN powder in DMF was prepared and mixed for 4 h at 40 °C. The solution was loaded in a plastic syringe with metal needle of 0.3 mm inner diameter. For electrospinning, the applied voltage was 10 kV, the flow rate was set

Open Access Article. Published on 12 Mac 2019. Downloaded on 3/09/2025 6:27:22 PTG.
This article is licensed under a Creative Commons Attribution-NonCommercial 3.0 Unported Licence.

at 0.5 mL h^{-1} and the distance between the needle tip and the aluminum collector was fixed at 15 cm in a vertical arrangement. Once obtained, PAN nanofibers were vacuum dried at 60 °C overnight. PAN nanofibers were modified with amidoxime groups (PAN-AO) by immersion in a 100 mL solution containing 0.8 g of $NH_2OH \cdot HCl$ and 0.6 g of Na_2CO_3 for 4 h at 30 °C. Then, PAN-AO nanofibers were washed with DI water and air dried overnight. Finally, PAN-AO was modified with –CHO groups by immersion in 100 mL of 2% w/w glutaraldehyde solution at room temperature with orbital shaking overnight. The final modified PAN support was labeled as mPAN (see photo of a typical membrane in ESI 1†).

Conformation of nanocomposite membranes and incorporation of Fe^{3+}. mPAN membranes were cross-linked with MCM-NH_2 and with MCM-PEI, separately. Membranes of 0.2 ± 0.01 g were immersed in a suspension of MCM-NH_2 or MCM-PEI in 50 mL of DI water. Cross-linking was carried out at room temperature with orbital shaking overnight. After the linking procedure, nanocomposites were washed several times with DI water to remove the non-linked nanoparticles. Nanocomposite membranes were labeled as mPAN/MCM-NH_2 and mPAN/MCM-PEI.

Incorporation of Fe^{3+} was done by immersion of the nanocomposites in a solution of 2 g of $Fe(NO_3)_3 \cdot 9H_2O$ in 40 mL of ethanol. This procedure was performed at room temperature, in a hermetically closed recipient by orbital shaking overnight. Subsequently, nanocomposites were washed several times with DI water in order to remove residual iron(III), and labeled as mPAN/MCM-NH_2-Fe^{3+} or mPAN/MCM-PEI-Fe^{3+}.

2.3. Characterization

Images of MCM-41 nanoparticles were taken using a High Resolution Transmission Electron Microscope (HR-TEM, JEOL 2100 FEG-TEM). Raw electrospun nanofibers and nanocomposite membranes were imaged with a Scanning Electron Microscope (Zeiss Ultra 55 SEM instrument). Zeta Potential for NPs was determined by Dynamic Light Scattering (DLS) using a Beckman Coulter™ Delsa Nano C particle analyzer, (Brea, CA, USA). Fourier Transform Infrared Spectroscopy (FTIR Nicolet Instruments model Avatar-100 equipped with ATR diamond at 303 K, Madison, WI, USA) was used to follow, step by step, the synthesis of nanoparticles, nanofibers and the cross-linking procedures.

2.4. Batch adsorption studies

Different arsenic solutions were prepared from a 1000 mg L^{-1} of As(v) standard stock solution obtained by the dilution of $Na_2HAsO_4 \cdot 7H_2O$ salt. All arsenic solutions were kept at pH 8. Batch adsorption experiments were carried out at room temperature and orbital shaking. Induced Coupled Plasma (ICP) technique was used to determine arsenic concentration (ICP-OES, iCAP 6500 Thermo Scientific). As(v) adsorption was tested in three different ways: (a) modified nanoparticles (MCM-NH_2 or MCM-PEI) suspension in 10 mL water was exposed to 1 mg L^{-1} of As(v). After 90 min, particles were separated by centrifugation at 12 000 rpm for 15 minutes and the remaining concentration of As in water was analyzed; (b) membranes (mPAN/MCM-NH_2 and mPAN/MCM-PEI) were immersed in a 100 mL solution of 1 mg L^{-1} As(v). After 90 min, a water sample was collected and analyzed; (c) membranes with incorporated Fe^{3+} (mPAN/MCM-NH_2-Fe^{3+} and mPAN/MCM-PEI-Fe^{3+}) were immersed in 100 mL solution of 1 mg L^{-1} As(v). Water samples were collected every 5 minutes during the adsorption process over 90 minutes and analyzed. The amount of modified nanoparticles (20 ± 2 mg) was kept constant for all experiments reported here.

3. Results and discussion

3.1. Nanocomposite characteristics

The crosslinking reaction scheme of the nanocomposites membranes is schematically represented in Scheme 1. To follow the incorporation of the functional groups, FTIR spectra were collected for the synthesized NPs (Fig. 1(a)). IR bands for MCM-41 are typical of mesoporous silica[26,28] with a wide band at 3380 cm^{-1} corresponding to O–H stretching. The adsorption at 1067 cm^{-1} is attributed to the transversal optic (TO) mode of the asymmetric vibration of Si–O–Si and at 960 cm^{-1} to Si–OH vibration. Upon functionalization, the Si–O–Si shifts to 1041 and 1050 cm^{-1} for MCM-NH_2 and MCM-PEI, respectively. Moreover, the absorption at 960 cm^{-1} is less intense due to the reaction of silanol groups with amino precursors. N–H stretching is found in the 3200–3500 cm^{-1} region, where it overlaps with O–H stretching. Amino groups appear between 1650–1465 cm^{-1} due to –NH_2 and N–H bending. More intense bands in MCM-PEI are due to higher primary and secondary amino groups present in PEI structure. Typical bands for –CH_2 and C–H stretching are observed between 2980 and 2830 cm^{-1}.

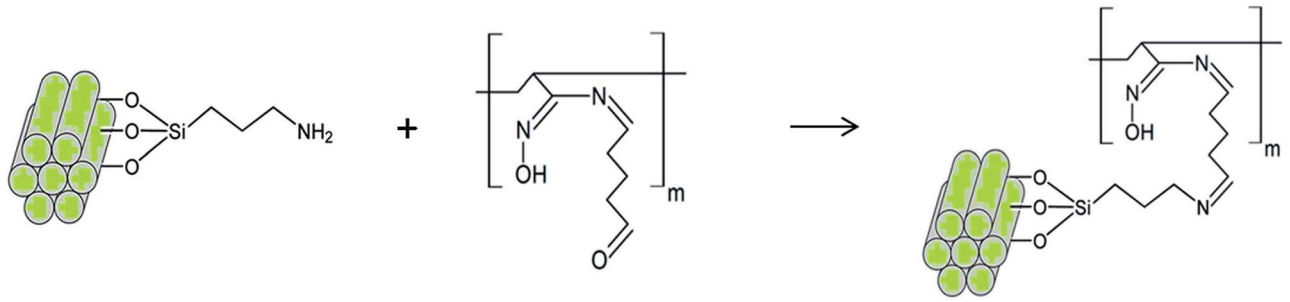

Scheme 1 Schematic representation of the cross-linking reaction between MCM-NH_2 and modified nanofibers (mPAN).

Open Access Article. Published on 12 Mac 2019. Downloaded on 3/09/2025 6:27:22 PTG.
This article is licensed under a Creative Commons Attribution-NonCommercial 3.0 Unported Licence.

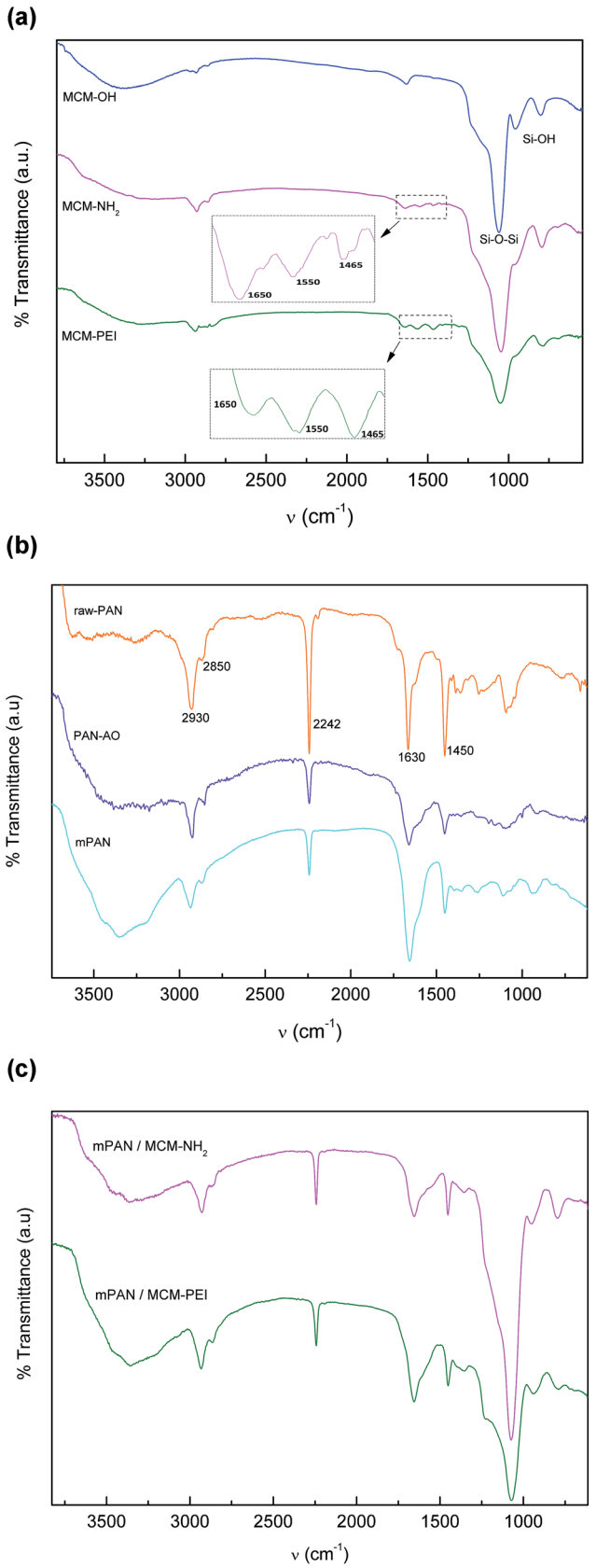

Fig. 1 (a) FTIR spectra of MCM-OH (—), MCM-NH_2 (—) and MCM-PEI (—). (b) FTIR spectra for raw-PAN (—), PAN-AO (—) and mPAN (—). (c) FTIR spectra for mPAN/MCM-NH_2 (—) and mPAN/MCM-PEI (—).

Fig. 1(b) shows PAN spectra during the synthesis steps. In electrospun raw nanofibers (raw-PAN), an intense band at 2242 cm^{-1} is observed that arise from C≡N stretching.[35] Peaks at 2933 cm^{-1} and 2850 cm^{-1} corresponding to $-CH_2-$ stretching and the one at 1455 cm^{-1} to bending vibration of C–H in $-CH_2-$ groups are also observed. Absorption band at 1630 cm^{-1} is possibly the vibration of the C=O bonds due to residual DMF solvent in the matrix.[35] After amidoxime functionalization (PAN-AO), the nitrite absorption at 2242 cm^{-1} becomes less intense suggesting that these groups are partially functionalized to amidoxime groups. In addition, a wide band appears around 3360 cm^{-1} due to overlapped N–H and O–H stretching vibrations. The wide band at 1655 cm^{-1} can be attributed to overlapped C=N and $-NH_2$ vibrations. In mPAN spectrum increased peak at 1655 cm^{-1} is due to contribution of both C=N and C=O stretching.

Fig. 1(c) shows spectra for mPAN/MCM-NH_2 and mPAN/MCM-PEI membranes. As it can be seen, cross-linking has been successfully achieved; in both cases, peak at 1655 cm^{-1} is less intense due to reaction of C=O of the modified nanofibers with $-NH_2$ groups from MCM-NH_2 or MCM-PEI nanoparticles. Moreover, the wide band between 3600–3000 cm^{-1} becomes less intense due to the lowering of N–H stretching groups. Absorption band at 1070 cm^{-1} is typically from Si–O–Si vibrations of silica nanoparticles.

Fig. 2 shows (a) HRTEM image of MCM-NH_2 and (b) HRTEM image of MCM-PEI. Rod-like functionalized nanoparticles with regular hexagonal structure are observed. Fig. 2(c), (d) and (e) presents SEM image of mPAN, mPAN/MCM-NH_2 and mPAN/MCM-PEI, respectively. Several authors had demonstrated that functionalization does not change mesoporous structure so no comparison has been carried out between as-synthesized and functionalized NPs.[26] SEM image shows the nanoparticles linked to nanofibers after the cross-linking step, due to covalent bonding as evidenced from FTIR analysis.

Zeta potential analyses of the different synthesized NPs were determined to confirm the functionalization with APTES and PEI precursors and to explain how the types of functionalization may be crucial for arsenic adsorption. ZP measurements were performed in water as a function of pH as shown in Fig. 3(a). For MCM-OH, surface charge is positive in acidic solution changing to negative in basic solution. The point of zero charge (pzc), or isoelectric point, corresponds to the condition where the electrical charge density on a surface is zero. In agreement with other reports, the point of zero charge (pH_{pzc}) was found at 5.8 for MCM-OH.[28] For amino functionalized NPs, the pH_{pzc} shifted towards basic region. pH_{pzc} was found to be 8.06 for MCM-NH_2 and 11.3 for MCM-PEI, similar to what has been reported in the literature.[36] The different pH_{pzc} values showed that functionalization has effects on the surface charge and that pH_{pzc} varies with the quantity of amine groups on the surface. Higher pH_{pzc} found for MCM-PEI than for MCM-NH_2 is consistent with the more amine groups present in PEI in comparison to APTES precursor. In acidic solutions, PEI is a polycation. According to Demadis *et al.*,[37] PEI bears primary (36%), secondary (27%) and tertiary (36%) amine groups, with pK_a values close to 4.5, 6.7 and 11.6, respectively. These results further justify the observations made during the FTIR studies.

Open Access Article. Published on 12 Mac 2019. Downloaded on 3/09/2025 6:27:22 PTG.
This article is licensed under a Creative Commons Attribution-NonCommercial 3.0 Unported Licence.

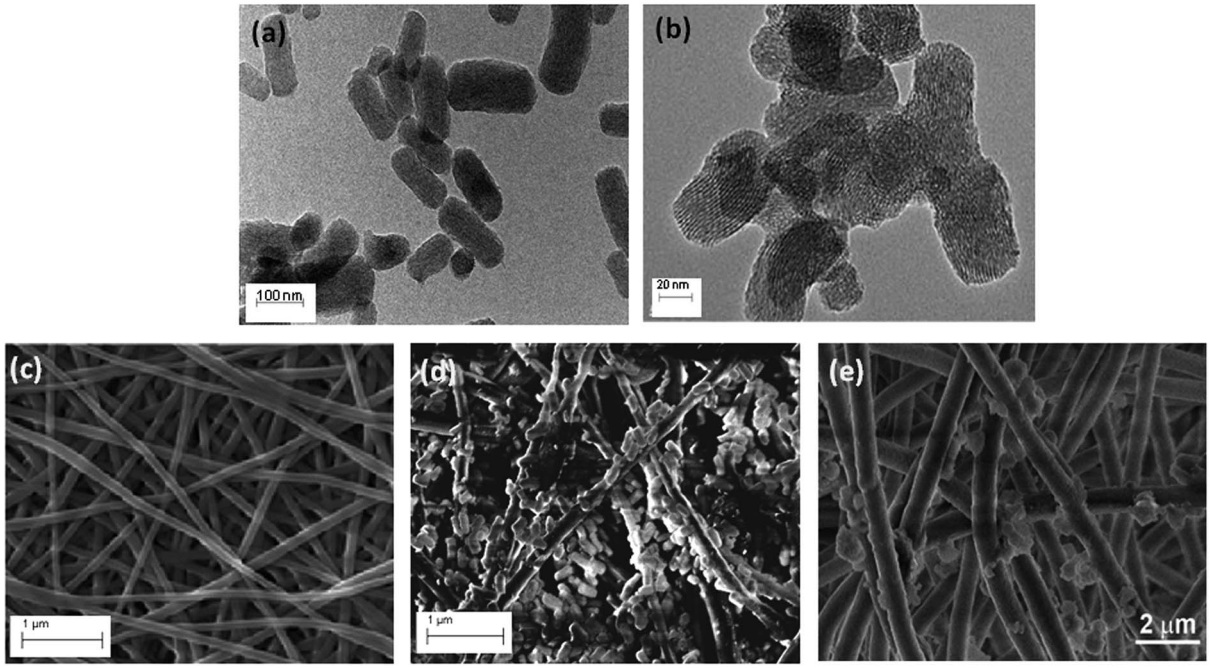

Fig. 2 HRTEM image for (a) MCM-NH_2, and (b) MCM-PEI; and SEM images for (c) mPAN, (d) mPAN/MCM-NH_2 and (e) mPAN/MCM-PEI nanocomposites.

Zeta potential was also investigated for nanocomposites as shown in Fig. 3(b). As can be observed from the data, the mPAN surface has a PZC at approximately pH 6.0, making it negatively charged (−19 mV) and hence ineffective as an arsenic adsorbent at pH 8. On the contrary, mPAN/MCM-PEI has a low positive charge at pH 8.0 (+1.52 mV), which correlates well and explains its higher relative adsorption as compared to mPAN/MCM-NH_2, which has a point-of-zero-charge at pH 4.2 and negative surface (−35 mV) at pH 8.0. The results here indicate that there is a moderate shift in the pH_{pzc} towards the acidic side for both mPAN/MCM-PEI and mPAN/MCM-NH_2 wherein the higher number of amine groups in PEI help in maintaining a more basic pH_{pzc}. Effectively, it appears that the mPAN surface charge screens some of the negative MCM particle charges, reducing the net adsorption capacity of the As(v) species. Nonetheless what is interesting to note here is that when the functionalized MCM particles are supported on mPAN membranes, their specific adsorption capacity is considerably enhanced as compared to their colloidal form, indicating that not all free surface functional groups contribute to the adsorption process in the colloidal solution.

3.2. Adsorption studies

Adsorption is a surface-based process and a consequence of surface energy. The exact nature of the bonding depends on the involved species, but the adsorption process is generally classified as physisorption (characteristic of weak van der Waals forces), chemisorption (characteristic of covalent bonding) or electrostatic attraction between the adsorbate and the adsorbent. According to Benhamou *et al.*,[28] large adsorption capacity of aminated materials may be explained by a local chemisorption mechanism between amines groups and As(v) species. Besides, pH of the solution is a critical parameter that rules arsenic removal since it may affect sorbent charge and arsenic speciation in solution. Arsenic is a triprotic acid that dissociates according to the following equations:[28]

$$H_3AsO_4 + H_2O \leftrightarrows H_2AsO_4^- + H_3O^+,\ pK_{a1} = 2.2 \quad (1)$$

$$H_2AsO_4^- + H_2O \leftrightarrows HAsO_4^{2-} + H_3O^+,\ pK_{a2} = 6.9 \quad (2)$$

$$HAsO_4^{2-} + H_2O \leftrightarrows AsO_4^{3-} + H_3O^+,\ pK_{a3} = 11.5 \quad (3)$$

Fig. 4 shows distribution of arsenic(v) species as a function of pH. Calculations were performed with Hydra/Medusa computer software[38] with an initial concentration of 1.33 10^{-5} mol L^{-1} (1 mg L^{-1}) of As(v). In the present work, arsenic solutions are studied at pH 8, simulating typical pH found in Argentinian groundwater,[13] where arsenic is mostly present in anionic form, $HAsO_4^{2-}$. Taking into account zeta potential values at pH 8, it is expected a neutral charge for MCM-NH_2 and a positive charge for MCM-PEI.

Adsorption capacity (q) was calculated using the following equation:

$$q = \frac{(C_i - C_e)}{W} V \quad (4)$$

where C_i (mg L^{-1}) and C_e (mg L^{-1}) are the initial and equilibrium concentrations of arsenic, respectively, V (L) is the volume of the arsenic solution and W (g) is the weight of nanoparticles linked to the nanofibers.

Adsorption tests performed with suspended MCM-NH_2 and MCM-PEI nanoparticles in As(v) solution at pH = 8 revealed a capacity concentration at equilibrium, q_e, of 0.003 mg g^{-1} with

Open Access Article. Published on 12 Mac 2019. Downloaded on 3/09/2025 6:27:22 PTG.
This article is licensed under a Creative Commons Attribution-NonCommercial 3.0 Unported Licence.

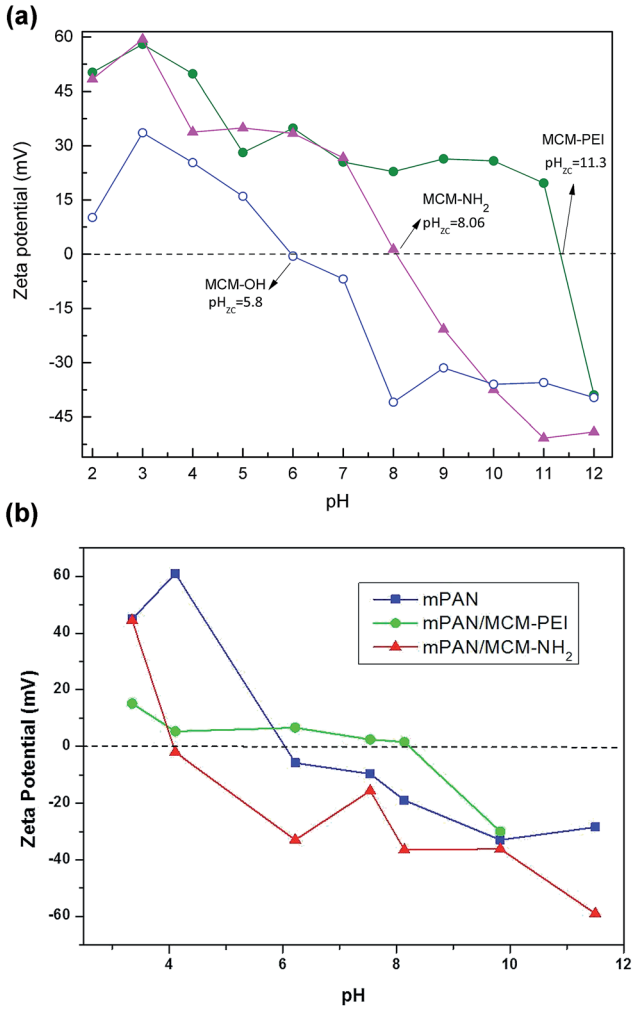

Fig. 3 Zeta potential and point-of-zero charge for (a) MCM-OH (—■—), MCM-NH$_2$ (—▲—) and MCM-PEI (—●—); (b) mPAN (—■—), mPAN/MCM-NH$_2$ (—▲—) and mPAN/MCM-PEI (—●—).

MCM-NH$_2$ and 0.053 mg g^{-1} with MCM-PEI within 90 min of adsorption. In this case, considering q_e and the charge of nanoparticles at pH 8, the higher and effective adsorption of arsenate species with MCM-PEI might be due to the negative charge of $HAsO_4^{2-}$ interacting with the positive charge of amino groups present in MCM-PEI nanoparticles. Contrary to the observations made by Benhamou *et al.*,[28] the positively charged surface of MCM-PEI nanoparticles are expected to provide better adsorption for negative arsenate ions ($HAsO_4^{2-}$) *via* electrostatic attraction.

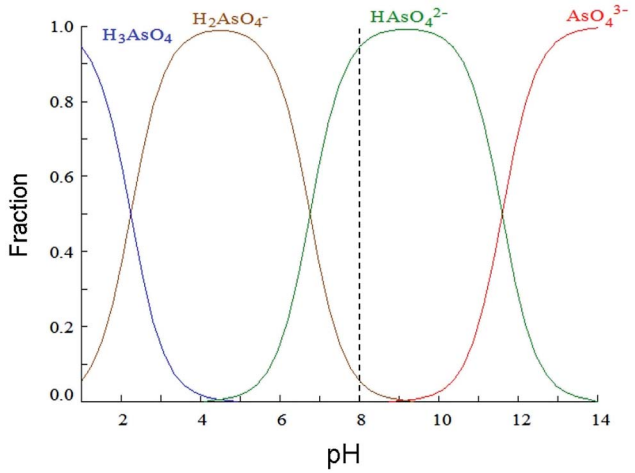

Fig. 4 Speciation of As(v) according to solution pH as determined using Medusa software.

It is important to consider that the adsorption of arsenic species with nanoparticles suspended in solution needs a further separation step, either centrifugation or filtration. This is inconvenient for applications in continuous flow reactors and is impractical since it would lead to higher complexities in operations. Moreover, suspended NPs tend to agglomerate in solution that has led to the studies of many immobilization matrices.[39] In this work, nanoparticles were cross-linked with functionalized nanofibers. Adsorption tests with these membranes were carried out in batch mode operation using orbital shaking as it has been described in Section 1.4. As stated before, the amount of nanoparticles linked to the nanofibers was 20 ± 2 mg in each case, which represents a 10% in weight of the adsorbent. Results of adsorption characteristics showed $q_e = 0.05$ mg g^{-1} for mPAN/MCM-NH$_2$ and $q_e = 1$ mg g^{-1} for mPAN/MCM-PEI. These values represent an increment of nearly twenty times of adsorbed arsenic compared to suspended nanoparticles, indicating that dispersed NPs on mPAN surface have higher efficiency in the adsorption of As(v). However, particles attached to the nanofibrous support lead to a reduction in the net positive charge which reduces $HAsO_4^{2-}$ adsorption.

To enhance the adsorption capacity further, membranes were treated with a Fe^{3+} solution. Fe^{3+} coordinated to amino ligands has been studied before by Yokoi *et al.*[24] where it was reported that Fe^{3+} acts as a strong adsorbent due to its high selectivity to arsenic(v). Fe^{3+} in solution is easily captured by amino ligands which work effectively as adsorption sites for metal cations.[40] Incorporation of Fe^{3+} has been studied by other authors as well.[30,41] In order to increase the percentage of arsenic adsorption, nanocomposites were treated with an excess amount of Fe^{3+} solution. Adsorption tests performed using mPAN/MCM-NH$_2$-Fe^{3+} and mPAN/MCM-PEI-Fe^{3+} membranes show substantial improvements. For comparison, Fig. 5(a) shows arsenic adsorption capacity obtained in each case studied after 90 minutes of exposure, where it can be seen the increase in the adsorption capacity of the nanocomposite membranes when treated with Fe^{3+}. These results showed that the presence of amino groups on surface are responsible for increasing density of Fe^{3+} which plays the main role for arsenic adsorption. Fig. 5(b) shows arsenic adsorption capacity as a function of time. For mPAN/MCM-NH$_2$-Fe^{3+} arsenic removal reached 87% in 15 minutes and 97% after 30 minutes. In the case of mPAN/MCM-PEI-Fe^{3+}, 95% removal was observed during the first 15 minutes and after 30 minutes practically all the arsenic was removed. The difference in the percentage of adsorption between mPAN/MCM-PEI-Fe^{3+} and mPAN/MCM-NH$_2$-Fe^{3+} shows that the presence of more amino groups on surface are responsible for increasing density of Fe^{3+} on surface, leading in an increment of the arsenic adsorbed.

Open Access Article. Published on 12 Mac 2019. Downloaded on 3/09/2025 6:27:22 PTG.
This article is licensed under a Creative Commons Attribution-NonCommercial 3.0 Unported Licence.

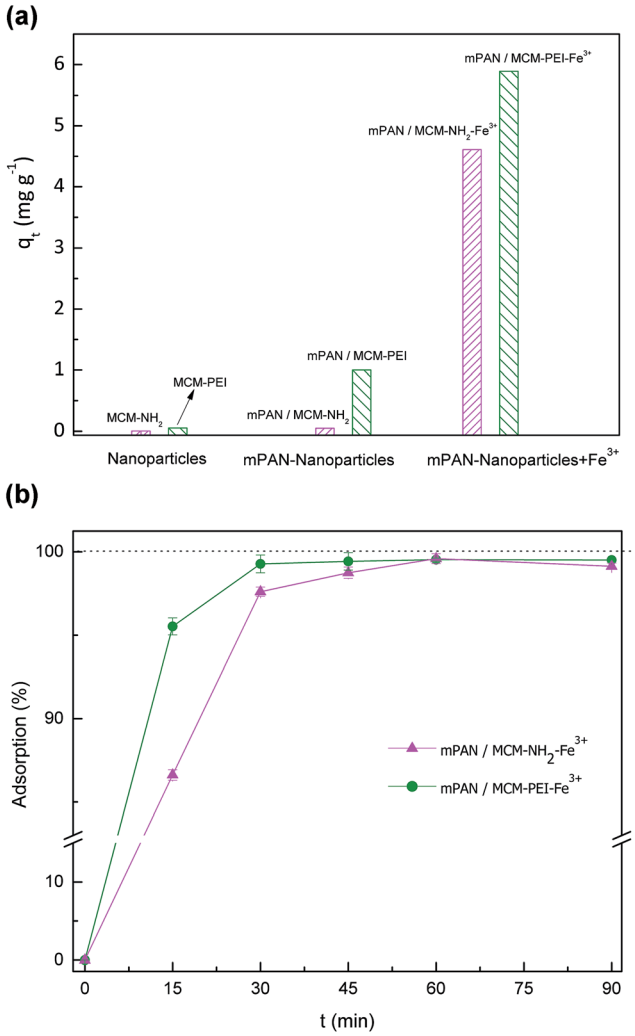

Fig. 5 (a) Adsorption percentage for comparison between nanoparticles, nanoparticles cross-linked to mPAN and with the incorporation of Fe^{3+}; and (b) adsorption percentage for mPAN/MCM-NH$_2$-Fe^{3+} (—▲—) and mPAN/MCM-PEI-Fe^{3+} (—●—) as a function of time.

3.3. Adsorption kinetics

Adsorption kinetics of As(v) was investigated in order to understand adsorption behavior. In Fig. 6 and 7, adsorption capacities (q) *versus* contact time are respectively shown for mPAN/MCM-NH$_2$-Fe^{3+} and mPAN/MCM-PEI-Fe^{3+} nanocomposites membranes. The adsorption capacity for As(v) removal rapidly reached 4.04 mg g^{-1} and 5.66 mg g^{-1} within the first 15 min for mPAN/MCM-NH$_2$-Fe^{3+} and mPAN/MCM-PEI-Fe^{3+}, respectively. It can be noticed that for mPAN/MCM-NH$_2$-Fe^{3+}, adsorption reached equilibrium after 45 min with a removal efficiency of 98.98% while for mPAN/MCM-PEI-Fe^{3+} the equilibrium was reached after 30 min with a removal efficiency of 99.6%. After 90 min of exposure, the amount of adsorbed arsenic was 4.61 mg g^{-1} for mPAN/MCM-NH$_2$-Fe^{3+} and 5.89 mg g^{-1} for mPAN/MCM-PEI-Fe^{3+}.

The obtained results show that the synthesized nanocomposites have a high adsorption efficiency and this characteristic is typical for porous adsorbents with high surface area and mesopore sizes that allow easy diffusion of arsenic species

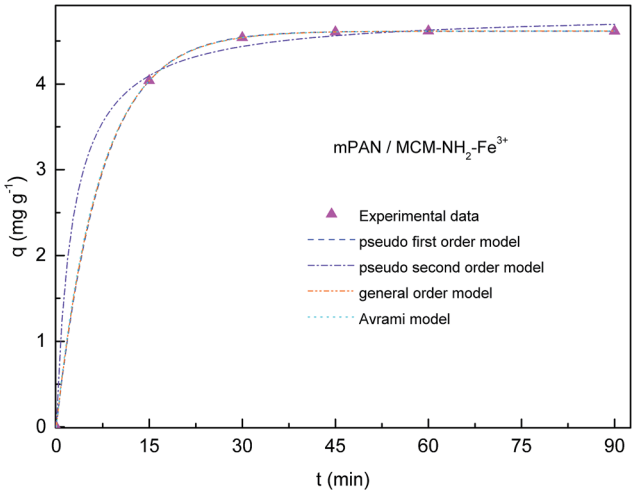

Fig. 6 Adsorption capacity for mPAN/MCM-NH$_2$-Fe^{3+}. Experimental data is represented by (▲). Dashed and dot lines represents kinetic models used for fitting. Experimental conditions: Initial concentration = 1 mg L^{-1}, adsorbent amount = 20 mg, pH = 8.

into the mesoporous channels.[42] High adsorption of As(v) on the surface of mPAN/MCM-NH$_2$-Fe^{3+} and mPAN/MCM-PEI-Fe^{3+} within a short time may be attributed to the availability of a large number of active binding sites (Fe^{3+}) on the surface of the nanoparticles attached to the nanofibrous support. The density of adsorbed Fe^{3+} increases with an increase in the surface density of the amino groups. These results are in agreement with a previously reported work.[24]

The experimental data was fitted using the nonlinear regression of pseudo-first order (eqn (5)), pseudo-second order (eqn (6)), general-order (eqn (7)) and the Avrami (eqn (8)) kinetic models:

$$q_t = q_{e,cal}(1 - \exp^{-k_1 t}) \quad (5)$$

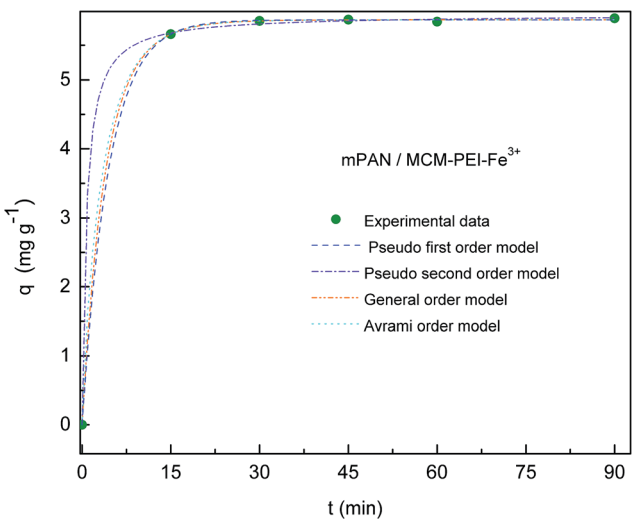

Fig. 7 Adsorption capacity for mPAN/MCM-PEI-Fe^{3+}. Experimental data is represented by (●). Dashed and dot lines represents kinetic models used for fitting. Experimental conditions: initial concentration = 1 mg L^{-1}, adsorbent amount = 20 mg, pH = 8.

Open Access Article. Published on 12 Mac 2019. Downloaded on 3/09/2025 6:27:22 PTG.
This article is licensed under a Creative Commons Attribution-NonCommercial 3.0 Unported Licence.

$$q_t = \frac{t}{\left(\frac{1}{k_2 q_{e,cal}^2}\right) + \left(\frac{t}{q_{e,cal}}\right)} \quad (6)$$

$$q_t = \frac{q_{e,cal}}{\left[k_N q_{e,cal}^{n-1}\ t(n-1)+1\right]^{1/(1-n)}} \quad (7)$$

$$q_t = q_{e,cal}\left(1 - \exp^{(-k_{AV} t)^{n_{AV}}}\right) \quad (8)$$

where k_1 is the pseudo-first order rate constant and k_2 is the pseudo-second order rate constant. k_N is the general-order rate constant (min^{-1} $(mg\ g^{-1})^{n-1}$), n is the order of adsorption mechanism, k_{AV} is the Avrami kinetic constant (min^{-1}) and n_{AV} is the fractional adsorption order related to the adsorption mechanism; while $q_{e,cal}$ is the calculated (theoretical) adsorption capacity at equilibrium and q_t is the adsorption capacity at time t.

The coefficient of determination (R^2), adjusted coefficient of determination (R_{adj}^2), and the standard deviation (SD) was used to test the best fitting of the kinetic model to the experimental data:

$$R^2 = \left(\frac{\sum_i^n \left(q_{i,exp} - \bar{q}_{exp}\right)^2 - \sum_i^n \left(q_{i,exp} - \bar{q}_{i,cal}\right)^2}{\sum_i^n \left(q_{i,exp} - \bar{q}_{exp}\right)^2}\right) \quad (9)$$

$$R_{adj}^2 = 1 - \left(1 - R^2\right)\left(\frac{n-1}{n-p-1}\right) \quad (10)$$

$$SD = \sqrt{\left(\frac{1}{n-p}\right)\sum_i^n \left(q_{i,exp} - q_{i,cal}\right)^2} \quad (11)$$

where $q_{i,cal}$ represents the individual theoretical q value predicted by the model; $q_{i,exp}$ represents the individual experimental q value; $\bar{q}_{exp}$ is the average of experimental q values; n represents the number of experiments; and p represents the number of parameters in the model.

Table 1 Kinetic parameters obtain for model fitting for the adsorption of As(v) onto to composite membranes

Experimental data for mPAN/MCM-NH_2-Fe^{3+} Amount adsorbed at equilibrium, $q_{e,exp}$ (mg g^{-1}) = 4.61	Experimental data for mPAN/MCM-PEI-Fe^{3+} Amount adsorbed at equilibrium, $q_{e,exp}$ (mg g^{-1}) = 5.89
Pseudo-first order model	
Rate constant, k_1 (min^{-1}) = 0.139 Amount adsorbed at equilibrium, $q_{e,cal}$ (mg g^{-1}) = 4.62 Adjust determination coefficient, R_{adj}^2 = 0.9998 Standard deviation, SD (mg g^{-1}) = 0.001	Rate constant, k_1 (min^{-1}) = 0.223 Amount adsorbed at equilibrium, $q_{e,cal}$ (mg g^{-1}) = 5.89 Adjust determination coefficient, R_{adj}^2 = 0.9999 Standard deviation, SD (mg g^{-1}) = 0.009
Pseudo-second order model	
Rate constant, k_1 (g mg^{-1} min^{-1}) = 0.077 Amount adsorbed at equilibrium, $q_{e,cal}$ (mg g^{-1}) = 4.84 Adjust determination coefficient, R_{adj}^2 = 0.9968 Standard deviation, SD (mg g^{-1}) = 0.069	Rate constant, k_1 (g mg^{-1} min^{-1}) = 0.0032 Amount adsorbed at equilibrium, $q_{e,cal}$ (mg g^{-1}) = 5.95 Adjust determination coefficient, R_{adj}^2 = 0.998 Standard deviation, SD (mg g^{-1}) = 0.026
General order model	
General rate constant, k_1 (min^{-1} (g mg^{-1})$^{n-1}$) = 0.138 Amount adsorbed at equilibrium, $q_{e,cal}$ (mg g^{-1}) = 4.62 Order kinetic adsorption, n = 1.02 Adjust determination coefficient, R_{adj}^2 = 0.9992 Standard deviation, SD (mg g^{-1}) =0.008	General rate constant, k_1 (min^{-1} (g mg^{-1})$^{n-1}$) = 0.147 Amount adsorbed at equilibrium, $q_{e,cal}$ (mg g^{-1}) = 5.87 Order kinetic adsorption, n = 1.09 Adjust determination coefficient, R_{adj}^2 = 0.9997 Standard deviation, SD (mg g^{-1}) =0.013
Avrami order model	
Avrami rate constant, k_1 (min^{-1}) = 0.139 Amount adsorbed at equilibrium, $q_{e,cal}$ (mg g^{-1}) = 4.62 Fractional adsorption order, n = 0.97 Adjust determination coefficient, R_{adj}^2 = 0.9996 Standard deviation, SD (mg g^{-1}) = 0.007	Avrami rate constant, k_1 (min^{-1}) = 0.281 Amount adsorbed at equilibrium, $q_{e,cal}$ (mg g^{-1}) = 5.87 Fractional adsorption order, n = 0.837 Adjust determination coefficient, R_{adj}^2 = 0.9998 Standard deviation, SD (mg g^{-1}) = 0.013

Open Access Article. Published on 12 Mac 2019. Downloaded on 3/09/2025 6:27:22 PTG.
This article is licensed under a Creative Commons Attribution-NonCommercial 3.0 Unported Licence.

In Table 1, kinetic parameters obtained from model fitting are presented. High R_{adj}^2 and low SD reveals good adjustment between experimental data and theoretical models. In this case, when comparing $q_{e,cal}$, $q_{e,exp}$, R_{adj}^2 and SD values between the different kinetic models, it can been seen that the pseudo first order model fits better to experimental data for both nanocomposite membranes studied, meaning that the rate-controlling step might be a physical process.[5,25]

However, kinetic models cannot be specifically used to determine an adsorption mechanism for the system under study. The prediction of the rate-limiting step is an important factor to be considered in the adsorption process. According to Rengaraj *et al.*[43] and Kalavathy *et al.*,[44] for the solid–liquid adsorption process, the solute transfer is characterized by external transfer and/or intra-particle diffusion, and the relative mechanisms of adsorption include three steps: (i) solute diffusion from bulk solution to the adsorbent exterior surface (external diffusion); (ii) diffusion of the adsorbate within the pores of the adsorbent (intra-particle diffusion); (iii) adsorption of the adsorbate onto active sites on the adsorbent. The last step is assumed to be fast, so it is negligible. To reach out a mechanism for As(v) adsorption, the intra-particle diffusion model can be investigated as proposed by Weber and Morris.[45] According to this theory, the adsorbate uptake, q_t, varies almost proportionately with the square root of contact time, $t^{1/2}$ rather than t, according to eqn (12):

$$q_t = K_i t^{1/2} + C \tag{12}$$

where K_i is the intra-particle diffusion rate constant (mg g^{-1} min$^{-0.5}$) and C is a constant related to the thickness of boundary layer (mg g^{-1}). If the rate-limiting step of arsenic diffusion is due to the intra-particle diffusion, then q_t *versus* $t^{1/2}$ should be linear and pass through the origin.

In this work, adsorption curves fitted with Weber and Morris model (see ESI 2†) do not follow a linear behavior suggesting that the intraparticle diffusion is not the dominant process determining the kinetics of the adsorption process.[29] Experimental data exhibit three linear zones suggesting that the overall adsorption process may indeed be controlled either by one or more steps, or a combination of steps. It is assumed that the first linear portion (zone 1) represents the diffusion process of mass transfer onto the adsorbent surface. The second linear portion (zone 2) is the gradual adsorption stage ascribed to intra-particle diffusion.[46] The third linear portion (zone 3) can be regarded as the diffusion through smaller pores, followed by the establishment of equilibrium.[47] Extended studies are being carried out to establish a possible mechanism for As(v) adsorption onto these nanocomposite membranes.

4. Conclusions

In this work, nanocomposite functionalized membranes were synthesized, characterized and tested for aqueous As(v) adsorption. Amino functionalized silica nanoparticles were cross-linked to functionalized polyacrylonitrile nanofibers, resulting in a homogenous nanocomposite fibrous membrane capable of removing As(v), fast and efficiently. Experiments showed low efficiency for arsenic adsorption using mPAN/MCM-NH_2 and mPAN/MCM-PEI. However, with the addition of small amounts of Fe^{3+}, adsorption reached almost 98% within the first 30 min. The equilibrium adsorption capacity for mPAN/MCM-NH_2-Fe^{3+} and mPAN/MCM-PEI-Fe^{3+} were 4.61 mg g^{-1} and 5.89 mg g^{-1}, respectively, both following a pseudo-first order kinetic model for adsorption process. Adsorption equilibrium was obtained within 30 min with mPAN/MCM-NH_2-Fe^{3+} and 15 min with mPAN/MCM-PEI-Fe^{3+}, the fast adsorption rate suggested that NH_2 groups were readily available and easily accessible. Thus, nanocomposite membranes synthesized in this work are easy to apply and effective materials for the adsorption As(v).

Conflicts of interest

There are no conflicts to declare.

Acknowledgements

This work has been supported by Argentina National Scientific and Technical Research Council (CONICET) and Nanoremovas project: H2020-MSCA-RISE-2014 [grant number 645024], "Advanced multifunctional nanostructured materials applied to remove arsenic in Argentinian groundwater".

References

1 B. K. Mandal and K. T. Suzuki, *Talanta*, 2002, **58**, 201–235.
2 WHO, *World Health Organization Guidelines*, 2011.
3 B. Emo, C. Eberlin, E. G. Kalaf, J. Laktas and S. Sell, *J. Environ. Chem. Eng.*, 2017, **5**, 232–239.
4 F. Cubadda, B. P. Jackson, K. L. Cottingham, Y. O. Van Horne and M. Kurzius-Spencer, *Sci. Total Environ.*, 2017, **579**, 1228–1239.
5 C. G. Lee, P. Alvarez, A. Nam, S.-J. Park, T. Do, U.-S. Choi and S.-H. Lee, *J. Hazard. Mater.*, 2017, **325**, 223–229.
6 USEPA, *National Primary Drinking Water Regulations*, United States Environmental Protection Agency, 2001.
7 M. I. Litter, *Rev. Soc. Argent. Endocrinol. Ginecol. Reprod.*, 2010, **17**, 5–10.
8 P. L. Smedley and D. G. Kinnirugh, Arsenic in goundwater and the environment, *Essentials of Medical Geology*, 2013, ch. 12, pp. 279–310.
9 M. Puntoriero, A. V Volpedo and A. Fernandez Cirelli, *Front. Environ. Sci.*, 2014, **2**, 1–5.
10 H. B. Nicolli, J. Bundschuh, J. W. Garcia, C. M. Falcon and J. S. Jean, *Water Res.*, 2010, **44**, 5589–5604.
11 B. K. Benitez and K. T. Suzuki, *Hidroarsenisismo Crónico Regional Endémico Módulo: Abatimiento del Arsénico*, Ministerio de Salud la Nación, Buenos Aires, Argentina, 1st edn, 2012.
12 A. E. Bardach, A. Ciapponi, N. Soto, M. R. Chaparro, M. Calderon, A. Briatore, N. Cadoppi, R. Tassara and M. I. Litter, *Sci. Total Environ.*, 2015, **538**, 802–816.

Open Access Article. Published on 12 Mac 2019. Downloaded on 3/09/2025 6:27:22 PTG.
This article is licensed under a Creative Commons Attribution-NonCommercial 3.0 Unported Licence.

13 A. Galli, O. Acosta, E. Planes, G. Pérez and M. Valiente, *[D1.2] Nanoremovas Progress Report-M18, GA 645024. Groundwater status in target area. Comparison vs. regional situation*, UAB, Universidad Autónoma de Barcelona (España)-INTI, Instituto Nacional de Tecnología Industrial, Argentina, 2016.
14 S. Kuppusamy, T. Palanisami, M. Megharaj, K. Venkateswarlu and R. Naidu, *Rev. Environ. Contam. Toxicol.*, 2016, **236**, 117–192.
15 M. Li, C. Wang and M. J. O'Connell, *Environ. Sci.: Nano*, 2015, **2**, 245–250.
16 K. Gupta, T. Basu and U. C. Ghosh, *J. Chem. Eng. Data*, 2009, **54**, 2222–2228.
17 K. Gupta, S. Saha and U. C. Ghosh, *J. Nanopart. Res.*, 2008, **10**, 1361–1368.
18 Y. Zhang, X. M. Dou, M. Yang, H. He, C. Y. Jing and Z. Y. Wu, *J. Hazard. Mater.*, 2010, **179**, 208–214.
19 S. Zhang, H. Niu, Y. Cai, X. Zhao and Y. Shi, *Chem. Eng. J.*, 2010, **158**, 599–607.
20 Z. Veličković, G. D. Vuković, A. D. Marinković, M.-S. Moldovan, A. A. Perić-Grujić, P. S. Uskoković and M. Đ. Ristić, *Chem. Eng. J.*, 2012, **181–182**, 174–181.
21 P. R. Aranda, I. Llorens, E. Perino, I. De Vito and J. Raba, *Environmental Nanotechnology, Monitoring and Management*, 2016, **5**, 21–26.
22 S. Vadahanambi, S. H. Lee, W. J. Kim and I. K. Oh, *Environ. Sci. Technol.*, 2013, **47**, 10510–10517.
23 K. Wantala, S. Sthiannopkao, B. Srinameb, N. Grisdanurak and K.-W. Kim, *J. Environ. Eng.*, 2012, **138**, 119–128.
24 T. Yokoi, T. Tatsumi and H. Yoshitake, *J. Colloid Interface Sci.*, 2004, **274**, 451–457.
25 H. Alijani and Z. Shariatinia, *Chemosphere*, 2017, **171**, 502–511.
26 Y. Wu, Y. Jin, J. Cao, P. Yilihan, Y. Wen and J. Zhou, *J. Ind. Eng. Chem.*, 2014, **20**, 2792–2800.
27 H. Yoshitake, T. Yokoi and T. Tatsumi, *Chem. Mater.*, 2002, **14**, 4603–4610.
28 A. Benhamou, J. P. Basly, M. Baudu, Z. Derriche and R. Hamacha, *J. Colloid Interface Sci.*, 2013, **404**, 135–139.
29 Y. Glocheux, A. B. Albadarin, J. Galán, E. Oyedoh, C. Mangwandi, C. Gérente, S. J. Allen and G. M. Walker, *Microporous Mesoporous Mater.*, 2014, **198**, 101–114.
30 S. El Mourabit, M. Guillot, G. Toquer, J. Cambedouzou, F. Goettmann and A. Gransjean, *RSC Adv.*, 2012, **2**, 10916–10924.
31 A. D. Dwivedi, N. D. Sanandiya, J. P. Singh, S. M. Husnain, K. H. Chae, D. S. Hwang and Y.-S. Chang, *ACS Sustainable Chem. Eng.*, 2017, **5**, 518–528.
32 D. Morillo, A. Uheida, G. Pérez, M. Muhammed and M. Valiente, *J. Colloid Interface Sci.*, 2015, **438**, 227–234.
33 M. A. Shannon, P. W. Bohn, M. Elimelech, J. G. Georgiadis, B. J. Mariñas and A. M. Mayes, *Nature*, 2008, **452**, 301–310.
34 W.-S. Hung, C.-H. Tsou, M. De Guzman, Q.-F. An, Y.-L. Liu, Y.-M. Zhang, C.-C. Hu, K.-R. Lee and J.-Y. Lai, *Chem. Mater.*, 2014, **26**, 2983–2990.
35 F. Huang, Y. Xu, S. Liao, D. yang, Y.-L. Hsieh and Q. Wei, *Materials*, 2013, **6**, 969–980.
36 J. M. Rosenholm, A. Penninkangas and M. Lindén, *Chem. Commun.*, 2006, **37**, 3909–3911.
37 K. D. Demadis, M. Paspalaki and J. Theodorou, *J. Ind. Eng. Chem.*, 2011, **50**, 5873–5876.
38 *Software Medusa Hydra, Chemical Equilibrium Diagrams*.
39 M. López-García, M. Martínez-Cabanas, T. Vilariño, P. Lodeiro, P. Rodríguez-Barro, R. Herrero and J. L. Barriada, *Chem. Eng. J.*, 2017, **311**, 117–125.
40 A. Cotton and G. Wilkinson, *Advanced Inorganic Chemistry*, Ed. Limusa, 1978, p. 1173.
41 H. Yoshitake and T. Yokoi, *Chem. Mater.*, 2003, **15**, 1713–1721.
42 M. S. Moorthy, D. J. Seo, H. J. Song, S. S. Parka and C. S. Ha, *J. Mater. Chem. A*, 2013, **1**, 12485–12496.
43 S. Rengaraj, J. W. Yeon, Y. Kim, Y. Jung, Y. K. Ha and W. H. Kim, *J. Hazard. Mater.*, 2007, **143**, 469–477.
44 M. H. Kalavathy, T. Karthikeyan, S. Rajgopal and L. R. Miranda, *J. Colloid Interface Sci.*, 2005, **292**, 354–362.
45 W. J. Weber and J. C. Morris, *Proc. 1st Int. Conf. Water Pollut. Symp.*, 1962, vol. 2, pp. 231–266.
46 P. N. Diagboya, B. I. Olu-Owolabi and K. O. Adebowale, *J. Environ. Manage.*, 2014, **146**, 42–49.
47 F. M. Machado, C. P. Bergmann, E. C. Lima, B. Royer, F. E. de Souza, I. M. Jauris, T. Calveted and S. B. Fagan, *Phys. Chem. Chem. Phys.*, 2012, **14**, 11139–11153.